optics

MDPI

Article

Ultrafast Phonon Decay in Complex Oxides

Chandra P. Neupane, Jeremy Sylvester, Dinusha M. S. R. Mudiyanselage, Helani A. S. Singhapurage and Feruz Ganikhanov *

Physics Department, University of Rhode Island, 2 Lippitt Dr, Kingston, RI 02881, USA
* Correspondence: fganikhanov@uri.edu

Abstract: The decay of multiple Raman active vibrations has been directly traced, in time, in technologically important wide bandgap semiconduction oxides such as $BaSnO_3$ (BSO), $STiO_3$ (STO), and $KTiOPO_4$ (KTP) crystal, which have important applications in laser frequency conversion. A time-domain coherent Raman technique, with excellent time (~120 fs) and spectral resolutions, has been applied to measure the ultrafast decay rates of optical phonons with 350–1500 cm^{-1} frequencies. Phonon decay mechanisms via phonon energy loss due to second- and third-order parametric processes have been discussed. The correspondingly high equivalent spectral resolution allowed for the determination of the phonon line bandwidths to be within 7.2–8.3 cm^{-1} (BSO), 8.5–9.7 cm^{-1} (STO), and 6.2–18.6 cm^{-1} (KTP).

Keywords: ultrafast spectroscopy; nonlinear optics; equilibrium phonons

Citation: Neupane, C.P.; Sylvester, J.; Mudiyanselage, D.M.S.R.; Singhapurage, H.A.S.; Ganikhanov, F. Ultrafast Phonon Decay in Complex Oxides. *Optics* **2022**, *3*, 438–446. https://doi.org/10.3390/opt3040037

Academic Editor: Thomas Seeger

Received: 22 September 2022
Accepted: 16 November 2022
Published: 21 November 2022

1. Introduction

Complex oxide materials are key elements behind a variety of important applications in electronics, fiber optics, coherent light sources, and light frequency conversion. Oxide properties, such as transparency in the optical range of frequencies, high direct bandgap, optical anisotropy, and carrier mobility, combined with high thermal conductivity, make them an exceptional class of materials suitable for technological applications. Strong interest in transparent ternary oxides, with perovskite structure and wide bandgap, is due to their potential uses in important device applications. These can range from transparent logic and memory devices to light-emitting diodes to applications in solar cells and flat panel displays. One of the crucial parameters for microelectronic logic device applications is the high electrical mobility of carriers at room temperature that oxides can provide, while retaining their properties at heterojunction interfaces. If one approaches this issue from the quantitative side, the best values for room temperature mobility and conductivity in the model perovskite oxide semiconductor $SrTiO_3$ (STO) is below 10 $cm^2/(Vs)$ and 500 $(\Omega \times cm)^{-1}$ [1]. Very recently, significantly higher room temperature mobility and the corresponding conductivity of bulk BaSnO3 (BSO) have been reported. Luo et al. [2] were the first to demonstrate that room temperature mobility can be higher than 100 $cm^2/(V \times s)$ in the n-doped BSO crystals with a carrier concentration of 8×10^{19} cm^{-3}. Later, as the research progressed, with key optimizations to the crystal growth process established, much higher mobility and conductivity (~320 $cm^2/(V \times s)$ and 4×10^3 $(\Omega \times cm)^{-1}$, respectively) have been demonstrated [2,3]. In addition, detailed studies of the material's band structure within STO and $LaAlO_3$ (LAO) heterojunctions resulted in conduction band offsets that favor modulation and polarization doping schemes that are essential for the use of these structures in power electronic applications. However, one major drawback is that the mobility drops to 150 $cm^2/(V \times s)$ for thin film samples. The latter represents the best currently achieved value [1] for BSO films grown on $PrScO_3$ substrates, while the BSO films grown on STO substrates show even lower carrier mobility values, within 80–120 $cm^2/(V \times s)$ [4]. The main mechanism that adversely impacts the carrier mobility parameter in epitaxially grown thin films are thought to be impurities and dislocations

induced by the substrate material due to lattice mismatch. The problem can be mitigated by using special doping techniques. This results in compensation effects, whereas mechanisms attributed to screened electron–phonon and carrier–carrier interactions can certainly play a major role regarding both bulk and thin film samples, depending on the doping level, temperature, and substrate interfaces. Eventually, transient properties of phonon-plasmon modes and carrier-phonon scattering mechanisms impose the fundamental limit on carrier mobility. All these mechanisms have been the subject of careful investigations, especially for III-V semiconducting systems [5,6]. Carrier scattering mechanisms are absolutely crucial in determining the mobility, as it follows from the basic dependence of the mobility (μ) on the carrier's effective scattering time (τ) and its effective mass (m^*), i.e., $\mu = e\tau/m^*$. In a defect-free bulk crystal, the only scattering mechanism that affects the mobility is inelastic electron-phonon scattering. Knowledge of mechanisms for polar phonon interactions and phonon decay routes in a system where the screening of ionic potential is relatively weak is very important. This provides key information and quantitative data that can be used to analyze the results for doped samples (for both bulk and thin films) and better quantify and estimate the impact of other scattering mechanisms. Experiments on phonon decay will help to test hypotheses and explain recent results for carrier transport as concerning factors that limit electronic mobility and conductivity that can be realistically attained in doped complex oxide systems.

Metal-oxide inorganic compounds have also shown wide applications in generating high-power coherent light. Among these are non-centrosymmetric materials, such as potassium titanyl phosphate ($KTiOPO_4$), potassium titanyl arsenate ($KTiOAsO_4$), and others with exceptionally high optical nonlinearity and transparency that stretch from UV (350 nm) to middle-infrared (3.5 μm) levels. The large electro-optic coefficient for the materials, the low dielectric constant, and the ion exchange properties also make them suitable for electro-optic [7] and waveguided laser devices [8]. The high nonlinear optical coefficient combined with high birefringence make these materials exceptionally attractive and widely used in IR-visible frequency conversion applications for the output of source lasers, especially from the backbone Nd-doped crystal based 1064 nm laser sources. Renewed interest in the materials came about due to stimulated Raman scattering (SRS) experiments based on a high third-order nonlinear gain due to the properties of the material's phonon spectra. Thus, the materials possess high second and third-order nonlinearity associated with several Raman active vibrations at a high-frequency range and are of interest from the standpoint of generating a frequency comb that would ultimately support attosecond waveforms [9]. Detailed knowledge of the properties of lattice vibrations (phonons) is thus important in light of the applications of this material as the nonlinear gain (second- and third-order) medium.

2. Materials and Methods

In this work, we present results for the direct measurement of the phonon decay in single-crystal cubic $BaSnO_3$ perovskite, paraelectric $SrTiO_3$, and $KTiOPO_4$ crystal. Ultrafast time resolution and excellent sensitivity of a specially designed version of the coherent anti-Stokes Raman scattering (CARS) spectroscopy technique provided valuable insight into the dynamics of multiple phonon lines within the frequency range of 350–1500 cm^{-1}. Time-domain coherent Raman spectroscopies have demonstrated impressive results in the past with regard to studying vibrational modes in liquids and solids, as well as in atomic/molecular media [10–15]. Our approach is based on using a high repetition rate and widely tunable sources that allow us to trace time-domain signals within a high dynamic range and obtain an equivalent spectral resolution as good as 0.1 cm^{-1}. In addition, the experimental approach has not yet been applied to the class of materials under study. Damping rates of the characteristic Raman active modes in the high-bandgap materials have been determined with excellent precision, which is not attainable using other experimental methods. The obtained information is valuable, both from the standpoint of problems in fundamental physics and understanding carrier transport properties, including

mechanisms that put limits on achieving high electronic mobility. Results on phonon decay in the KTP crystal are also important, as they provide guidance when designing laser systems with frequency conversion.

The CARS process, with ultrashort pulses and time resolution, can be considered as a scattering of the probe pulse ($E_3(t)$) on the coherent excitation in a material created by the first two pulses ($E_1(t)$, $E_2(t)$) in the vicinity of Raman resonances. In this approach, for time-resolved measurements, excitation and probing processes are separated in time by a delay (t_d), and the time-dependent nonlinear polarization can be expressed with the help of the coherent amplitude (Q) created in the material, characterized by an atomic/molecular density N and polarizability tensor α [16]:

$$P_{as}^{(3)}(z, t - t_d) = N\frac{\partial \alpha}{\partial q}\frac{i}{2} Q(z,t)E_{30}(t - t_d)e^{i[(\omega_1-\omega_2+\omega_3)t-(k_1-k_2+k_3)z]}e^{-i\omega_3 t_d} \quad (1)$$

The detected wave is at the anti-Stokes frequency ($\omega_{as} = \omega_1 - \omega_2 + \omega_3$) with the corresponding field amplitude E_{as}. To efficiently drive lattice vibrations, frequencies ω_1 and ω_2 should be tuned so that the difference ($\omega_1 - \omega_2$) matches the characteristic lattice vibration (phonon) frequency (Ω_R). The transient value of $Q(t)$ is found from relevant equations [12,16] that account for the driving force for vibration and relaxation mechanisms quantified by a time constant T_2. The solutions for $Q(t)$ and the time-dependent CARS signal $S(t_d)$ are given by the following equations:

$$Q(z, t) = \sum_i q_i(z, t) \quad (2)$$

$$\left(\frac{\partial}{\partial t} + \frac{1}{T_2}\right) Q(t) = \kappa_Q E_1(t)E_2^*(t) \quad (3)$$

$$Q(z, t) = e^{-\frac{t}{T_2}} \int_{-t_0}^{+\infty} e^{-\frac{\theta}{T_2}} E_1(\theta)E_2{}^*(\theta)\kappa_Q H(t - \theta)d\theta \quad (4)$$

$$S(t_d) = \zeta \int_{-\infty}^{+\infty} \left| \int_0^L P(z, \quad t - t_d)dz \right|^2 dt \quad (5)$$

In the equations above, k_Q is the driving fields-to-material coupling constant, $H(t)$ is Heaviside's step function, E_1 and E_2 are the pulsed fields with the central frequencies ω_1, ω_2 that drive specific vibration(s) at a difference frequency $\omega_1 - \omega_2 \sim \Omega_R$, and Q is the macroscopic coherent amplitude within the effective focused fields volume. In the case of high-quality crystals, the phase of the individual vibrations $q_i(t)$ (in Equation (2)) is not changed after the pulsed excitation and therefore, one can effectively measure the time-dependent change in the amplitude of $q_i(t)$. The T_2 time constant effectively represents the phonon amplitude decay time. This is the case for homogenously broadened Raman active vibrations, and the corresponding linewidth for the homogenously broadened mode is $\Delta\nu\left[cm^{-1}\right] = 1/(\pi c T_2)$. The time-dependent CARS signals can be modeled using the theoretical approach outlined by Equations (1)–(5). The experimental results (Figures 2–4) have been fitted using Equations (1)–(4), the final expression (Equation (5)) for $S(t_d)$, and by varying the T_2 time constant until the best fit was found.

Figure 1 provides the main details of the experimental setup. The laser portion of the experimental layout is based on a high-power, mode-locked Ti: sapphire oscillator delivering 120 fs pulses (~30 nJ/pulse) at a 76 MHz repetition rate. The output is split into three parts. Two equal parts (~1 W each) of the output simultaneously pump lab-built, widely tunable optical parametric oscillators ($OPO_{1,2}$). The OPOs are widely tunable; the OPO_1 wavelength is maintained at approximately 1015 nm (λ_1), while the OPO_2 output can be tuned within 1030–1250 nm (λ_2). λ_1 and λ_2 correspond to ω_1 and ω_2, the optical frequencies required for CARS. Other details for the OPOs operation and their characteristics are provided in Refs. [17,18]. The third portion (~150 mW) of the Ti: S output is used as $E_3(t)$—pulse (or probe) beam. Two dichroic mirrors are used to spatially overlap

the three outputs—$OPO_{1,2}$ and the probe—while the delay stage is used to temporally overlap the pulses. The wavelengths and spectra are monitored with an optical spectrum analyzer (OSA). The three beams are focused with an objective lens (NA = 1.2) onto the sample to produce a CARS signal within a small volume (200 × 550 nm^2 rotational ellipsoid). In the described arrangement, $E_{1,2}(t)$ pulses, delivered by $OPO_{1,2}$, create a macroscopic coherence (with an amplitude Q) within the sample material. The delayed probe pulse probes the time evolution of the coherence at successive delay times. Within the signal detection portion, the generated CARS signal, at a wavelength of λ_{as}, is directed through a condenser, attenuator and lens trail, into a diffraction grating monochromator, and finally, into a cooled CCD detector. Spectrally and time-resolved CARS signal data are acquired and recorded with the help of the LabView program and a PC to provide real-time monitoring and data recording during the experiments. The spectrally and time-resolved CARS signal can be traced in time within nearly 80 dB, with better than 120 fs time resolution [19].

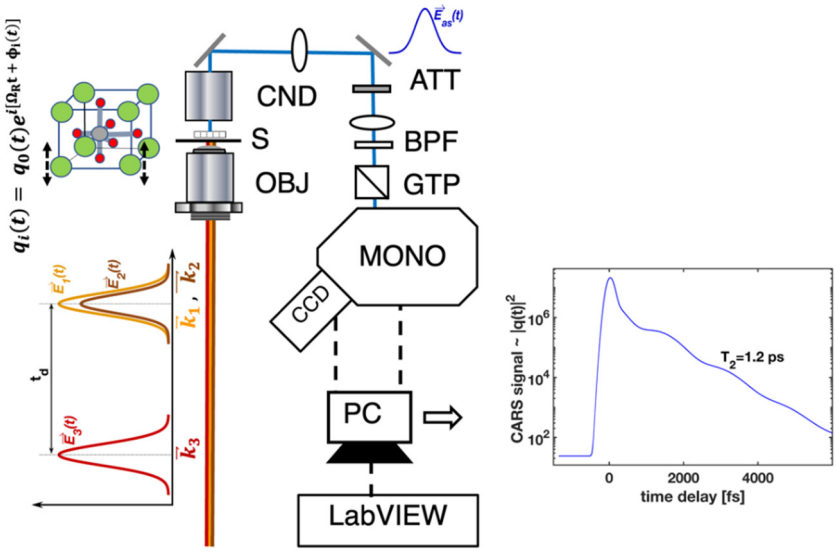

Figure 1. Schematic of the experimental setup. Pulsed fields $E_{1,2}$ (t) are used to coherently drive lattice vibrations at a specific frequency Ω_R. The $E_1(t)$ field is provided by a pulsed femtosecond OPO_1. $E_2(t)$—pulse wavelength can be tuned within a broad range to match a specific lattice vibration frequency ($\Omega_R = \omega_1 - \omega_2$). The $E_3(t - t_d)$ pulse (at 814 nm) probes the remaining coherence ($Q(t) = \sum_{i=1}^{N} q_i(t)$) within the focusing volume created by NA = 1.2 objective lens (OBJ). CCD detects the CARS signal at the anti-Stokes wavelength λ_{as}. S—sample, CND—condenser lens, ATT—light intensity attenuator, BPF—bandpass filter, GTP—Glan–Thompson prism polarizer, MONO—diffraction grating monochromator.

3. Results and Discussions

Figure 2a,b show CARS transients measured in cubic $BaSnO_3$ (BSO) single crystal. In these measurements, the phonon modes at ~465 cm^{-1} and ~630 cm^{-1} have been targeted. Analyzing spectral data using DFT studies shows that the detected signals correspond to the LO_2 and LO_3 modes. The time-resolved CARS spectra corresponding to the CARS transient in Figure 2a (red circles) representing the LO_2 mode are shown in Figure 2c, and the time-resolved CARS spectra corresponding to the CARS transient in Figure 2b (blue circles) representing the LO_3 phonon mode are shown in Figure 2d. The decay constant related to the corresponding CARS transients can be precisely obtained by fitting the experimental data for the time-resolved CARS signal with a theoretical model described by Equations (1)–(5). The initial ultrafast decay near the zero-delay time in Figure 2a,b is time (pulse width) resolution limited and is due to the non-resonant third-order electronic nonlinearity with an equivalent T_2 time less than a few fs [20]. Opposite to that, the slower decaying portion of a transient CARS date corresponds to the resonant third-order optical

nonlinearity due to the driven Raman active mode(s). The phase-matching is an important parameter to generate maximized intensity levels for CARS signals. However, in the tight beam focusing case (i.e., $0.25 \times 0.25 \times 0.7$ μm^3), the phase-matching condition is relaxed due to the short interaction length (L~0.7 μm) so that $\Delta k \times L << 1$. The intensity noise in our measurements is determined by intensity fluctuations for the three fields, and it is estimated to be less than <6% rms. Variations in pulse-to-pulse width are believed to be lower than a few percentage points. The ratio between the resonant and non-resonant components of the signal indicates the strength of the Raman active resonances. The CARS transient in Figure 2a,b shows a perfect exponential decay corresponding to the probed phonons at different frequencies. Fitting these experimental data with the theoretical model predicts the decay constants at room temperature $T_2 = 1.26 \pm 0.03$ ps and $T_2 = 1.47 \pm 0.03$ ps, corresponding to Figure 2a,b, respectively. The signal decay constant (T_2) yields the corresponding damping rates $(\Gamma = 2/T_2)$ and linewidths for the Raman active vibrations. The linewidths corresponding to the LO_2 and LO_3 phonons are 8.25 ± 0.12 cm^{-1} and 7.22 ± 0.08 cm^{-1}, respectively, with a spectral resolution of better than 0.15 cm^{-1}. Both the phase (dephasing) and amplitude slips of the phonon vibration play a key role and determine the time-domain behavior of the CARS transients. However, lattice vibration phase shifts can be neglected in our case, as we have a high-quality crystal in which the spatial disorder and free residual carrier concentrations are under control and thus, very small. Therefore, the pure dephasing mechanism is not contributing, in this case. The amplitude evolution in time for the phonon modes is determined by the efficiency of the phonon interactions due to the anharmonicity of the crystal potential.

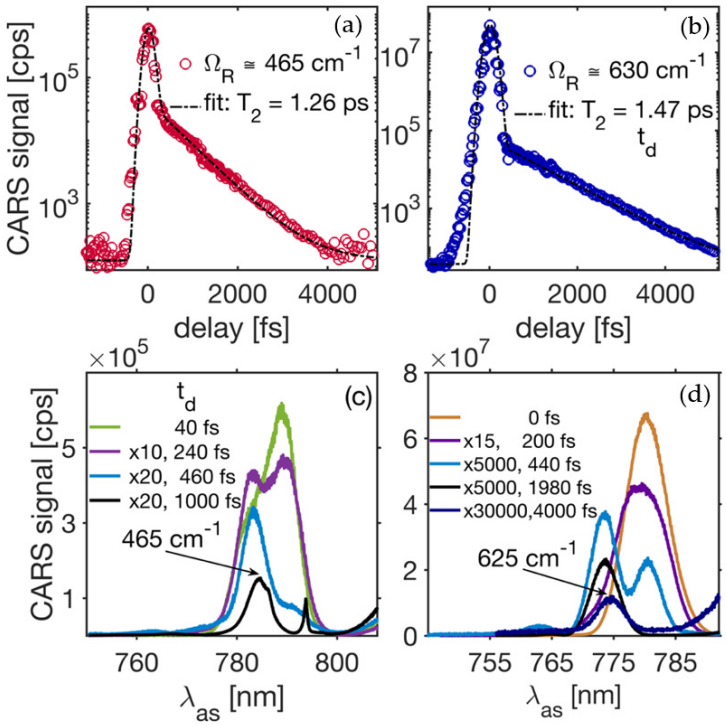

Figure 2. CARS transients obtained from cubic $BaSnO_3$ crystal while favoring LO_2 (**a**) and LO_3 (**b**) phonon mode excitations. For these cases, the OPO_1 central wavelength was fixed at 1015 nm, and the OPO_2 wavelengths were tuned to ~1065 nm and ~1073 nm, correspondingly. The CARS signals have been detected and monitored at the anti-Stokes wavelengths indicated by arrows on the spectral data, shown in parts (**c**,**d**), correspondingly. Dash-dotted lines correspond to the best fitting results using the theoretical model presented by formulas (1)–(3). The phonon decay time constant values (T_2) that resulted in the best fit are indicated in the legend.

The decay of a zone-center (Γ-point) LO-phonon into other phonons is treated in terms of the lowest-order anharmonic term in the crystal potential [21]. Here, the zero-wavevector

phonons normally decay into phonons of lower energy and opposite wavevectors, so that both the energy and the momentum are conserved within the process. The most probable decay path for the traced 465 cm^{-1} phonon (LO_2) in our CARS experiment is to split into zone-edge phonons of lower energy (~300 cm^{-1} and 160 cm^{-1}) that have opposite wavevectors. With this assumption, we can estimate that the zero-temperature linewidth, which is directly connected to the anharmonic potential's third derivative [21], is 3.89 cm^{-1}. The latter was with the help of the $\Delta v[cm^{-1}] = \Gamma/2\pi c$ relationship between the linewidth (Δv) and the decay rate (Γ) as the linewidth parameter is more commonly used and analyzed in spectroscopy. The LO_3 (~630 cm^{-1}) vibration matches well with the theoretical predictions for its frequency [22,23]. The density functional theory (DFT) results of [22] show that two momentum- and energy-conserving decay channels are possible. The possible overtone paths will result in final phonons with equal energy (315 cm^{-1}) and opposite wavevectors, while the combination channel involves two LO-phonons with energies of 480 cm^{-1} and 160 cm^{-1}. Moreover, there are decay paths that involve a pair of LO- and TO-vibrations with energies around 385 cm^{-1} and 240 cm^{-1}, as well as a path that results in the final phonon states at ~490 cm^{-1} and ~140 cm^{-1}. The above arguments, combined with data presented in Figure 2b for the ~630 cm^{-1} mode, yield the decay rate at zero-temperature to be within 0.63–0.89 ps^{-1} (or 2.38–3.36 cm^{-1} for the linewidths).

Figure 3 shows the time-domain CARS data from the $SrTiO_3$ single crystal. Two different phonon lines have been assigned as the main LO_3 and LO_4 zone center phonons in earlier works [24–26], although the anti-stokes wavelength appears to be somewhat blue-shifted in our experiment.

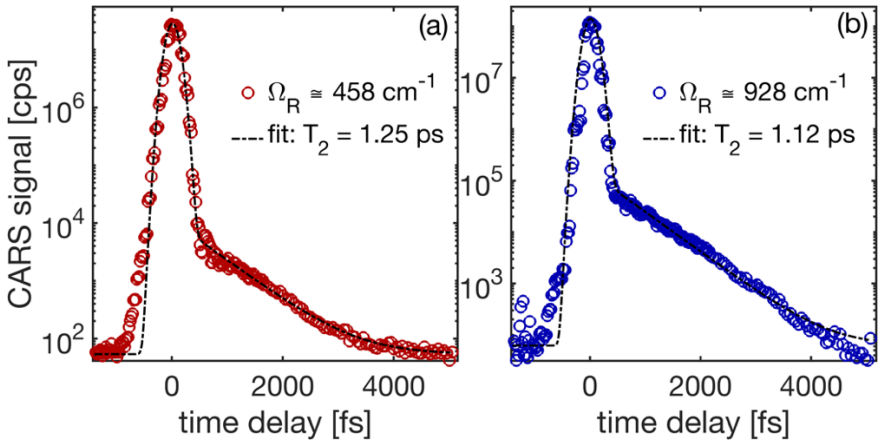

Figure 3. The time-resolved CARS signals obtained from the $SrTiO_3$ single crystal while favoring LO_3 (**a**) and LO_4 (**b**) phonon mode excitations. The OPO_1 central wavelength was fixed at ~1015 nm, while the OPO_2 wavelengths were tuned to ~1063 nm and ~1109 nm, correspondingly. The phonon decay time constant values (T_2), indicated in the legend, were obtained from the best-fitting results (dash-dotted curves).

The two-phonon state (LO_1 + LO_4) that is close to the high-frequency phonon data (Figure 3b) is believed to be broad [24] and therefore, should have resulted in a much faster phonon decay time (T_2). Based on the available data, we conclude that the LO_3 phonon decay is via the phonon split into the LO_1 (~173 cm^{-1}) and LO_2 (~265 cm^{-1}) phonons, resulting in the zero-temperature decay rate of 0.86 ps^{-1} (linewidth of ~4.6 cm^{-1}). The detected LO_4 phonon decay appears to be slightly faster, which we explain by the existence of a few different decay channels. Among these is the direct overtone channel that results in two LO_3 phonons that exhibit higher phonon density states, as well as a few other channels that involve parametric interactions of higher order with TO_4 (~550 cm^{-1}) and $LO_{1,2}$ and $TO_{2,3}$ phonons of lower energies.

Figure 4 presents time-domain CARS data obtained from KTP ($KTiOPO_4$) crystal when targeting vibrations around ~724 cm^{-1} and ~995 cm^{-1}. The flux-grown KTP crystal used

in the experiment was cut at f = 40° and q = 90°. Therefore, all four A_1–A_4 symmetry tensor components can be involved. The crystal's multiatomic unit cell makes the lattice spectra complex, as it can consist of about one hundred Raman active peaks, and the phonon line assignments may bring ambiguous results. However, contributions to Raman and infrared spectra from major atomic units within the primitive cell, as represented by TiO_6 octahedra and PO_4 tetrahedra, have been elucidated from previous studies [27–29]. We must note that the KTP Raman spectra in the vicinity of 650–850 cm^{-1} have shown a rich structure consisting of several strong Raman active lines. We have been able to differentiate between them by resolving the components spectrally within the anti-Stokes spectra and separately tracing the CARS signal decay in the time domain. The resonant contribution for the excited and probed ~830 cm^{-1} mode, shown in Figure 4a, is dominant, as the time resolution limited peak is absent. The experimental CARS signal shows nearly perfect exponential decay, with close to a straight-line signal trend (on the semilogarithmic plot) for over four decades. The exponential decay over several orders of magnitude proves that the Raman line is homogenously broadened. Indeed, the Fourier-transform calculations [30] for the CARS signal show less than a percent deviation from the Lorentzian line shape. The decay rate, obtained from the best-fitting results and shown as a dashed line in Figure 4a, indicates a T_2 time constant of 470 fs. The corresponding homogeneous linewidth is Δv = 22.6 cm^{-1}. Again, we stress that the line broadening is solely due to the loss of vibrational energy to other (lower energy) vibrational modes. The fast decay rate (broad linewidth) is explained by the fact that the final phonon states are the ones with high density, and that this is the main factor for the fast 824 cm^{-1} phonon decay rate compared to other modes. The latter are presented with an example of probing the lattice vibration mode at ~995 cm^{-1}. The mode is substantially weaker, as can be seen by a strong enough non-resonant contribution to the signal compared to the lower and much slower decaying resonant portion. The corresponding T_2 time is found to be 1.58 ps, which results in a linewidth of 6.7 cm^{-1}. We believe that the decay paths into lower energy phonon modes are impeded by a lack of channels with high enough density of states for the final phonons of ~ 400–600 cm^{-1} energy.

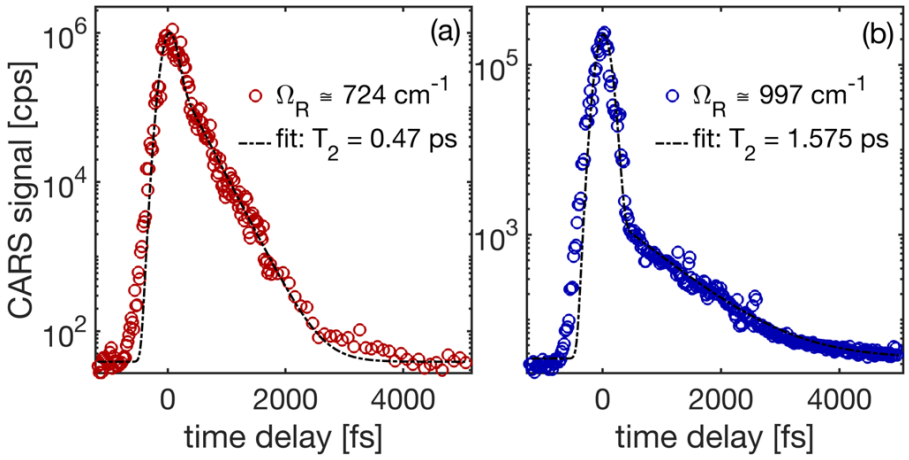

Figure 4. CARS transients obtained from $KTiOPO_4$ crystal while exciting and probing closely spaced strong (**a**) and weak (**b**) lattice vibration modes within the Ti-O octahedron of the crystal's elementary lattice unit. The OPO_1 central wavelength was fixed at ~1015 nm, while the OPO_2 wavelengths have been tuned to ~1097 nm and ~1136 nm, correspondingly, to facilitate the phonon excitations. The phonon decay time constant values T_2, indicated in the legend, are obtained from the best-fitting results (dash-dotted curves).

4. Conclusions

In conclusion, the decay of Raman active modes associated with metal-oxide vibrations within the unit cells has been traced in two transparent semiconducting crystals (BSO, STO), as well as in a nonlinear optical material, KTP crystal, that is used for laser frequency

conversion using time-domain CARS spectroscopy with 120 fs resolution. By analyzing phonon decay times and possible decay paths for the probed lattice vibrations, we provided estimates for zero-temperature decay rates for the primary LO-phonons. In particular, we found that the zero-temperature linewidths are on the order of 2.4–3.9 cm^{-1} for BSO, 5.8–6.4 cm^{-1} for STO, and 3.8–11.4 cm^{-1} for KTP. We believe that the phonon decay rate (or linewidth) is a key material parameter that affects the electronic and optical characteristics of the materials that are being used in important applications.

Author Contributions: Conceptualization, F.G.; methodology, C.P.N., J.S., H.A.S.S. and D.M.S.R.M.; software, D.M.S.R.M.; validation, C.P.N., J.S., H.A.S.S., D.M.S.R.M. and F.G.; formal analysis, C.P.N., H.A.S.S. and D.M.S.R.M.; investigation, C.P.N. and J.S.; resources, F.G.; data curation, C.P.N. and F.G.; writing—original draft preparation, C.P.N.; writing—review and editing, J.S., D.M.S.R.M., H.A.S.S. and F.G.; supervision, F.G.; project administration, F.G.; funding acquisition, F.G. All authors have read and agreed to the published version of the manuscript.

Funding: This material is based upon the work supported by the United States Air Force Office of Scientific Research under Award No. FA9550-18-1-0273.

Data Availability Statement: Data can be made available upon a reasonable request by contacting the corresponding author.

Acknowledgments: The authors thank the Department of Physics, University of Rhode Island, for material and logistical support.

Conflicts of Interest: The authors declare no conflict of interest.

References

1. Chambers, S.A.; Kaspar, T.C.; Prakash, A.; Haugstad, G.; Jalan, B. Band Alignment at epitaxial $BaSnO_3/SrTiO_3$ (001) and $BaSnO_3/LaAlO_3$ (oo1) heterojunctions. *Appl. Phys. Lett.* **2016**, *108*, 152104. [CrossRef]
2. Luo, X.; Oh, Y.S.; Sirenko, A.; Gao, P.; Tyson, T.A.; Char, K.; Cheong, S. High carrier mobility in transparent $Ba_{1-x}La_xSnO_3$ crystals with a wide band gap. *Appl. Phys. Lett.* **2012**, *100*, 172112. [CrossRef]
3. Niedermeier, C.A.; Kumagai, Y.; Ide, K.; Katase, T.; Oba, F.; Hosono, H.; Kamiya, T. Phonon scattering limited mobility in the representative cubic perovskite semiconductors $SrGeO_3$, $BaSnO_3$, and $SrTiO_3$. *Phys. Rev. B* **2020**, *101*, 125206. [CrossRef]
4. Yang, F.; Huang, L.; Zhao, X.; Huang, L.; Gao, D.; Bi, J.; Wang, X.; Zou, G. An energy band engineering design to enlarge the band gap of $KTiOPO_4$ (KTP)-type sulfates via aliovalent substitution. *J. Mater. Chem. C* **2019**, *7*, 8131–8138. [CrossRef]
5. Moore, E.J. Quantum-Transport Theories and Multiple Scattering in Doped Semiconductors. II. Mobility of n-type Gallium Arsenide. *Phys. Rev.* **1967**, *160*, 618. [CrossRef]
6. Meyer, J.R.; Bartoli, F.J. Ionized-impurity scattering in the strong-screening limit. *Phys. Rev. B* **1987**, *36*, 5989. [CrossRef]
7. Wang, X.D.; Basseras, P.; Miller, R.J.D.; Vanherzelle, H. Investigation of $KTiOPO_4$ as an electro-optic amplitude modulator. *Appl. Phys. Lett.* **1991**, *59*, 519. [CrossRef]
8. Savatinova, I.; Savova, I.; Liarokapis, E.; Ziling, C.C.; Atuchin, V.V.; Armenisek, M.N. A comparative analysis of Rb:KTP and Cs:KTP optical waveguides. *J. Phys. D Appl. Phys.* **1998**, *31*, 1667. [CrossRef]
9. Baker, S.; Walmsley, I.; Tisch, J.W.G.; Marangos, J.P. Femtosecond to attosecond light pulses from a molecular modulator. *Nat. Photonics* **2011**, *5*, 664–667. [CrossRef]
10. Alfano, R.; Shapiro, S. Optical phonon lifetime measured directly with picosecond pulses. *Phys. Rev. Lett.* **1971**, *26*, 1247. [CrossRef]
11. Laubereau, A.; Kaiser, W. Vibrational dynamics of liquids and solids investigated by picosecond light pulses. *Rev. Mod. Phys.* **1978**, *50*, 607. [CrossRef]
12. Vallee, F.; Gale, G.M.; Flytzanis, C. Biphonon dynamics in crystals: Nitrous oxide. *Chem. Phys. Lett.* **1986**, *124*, 216–219. [CrossRef]
13. Dlott, D.D. Optical phonon dynamics in molecular crystals. *Annu. Rev. Phys. Chem.* **1986**, *37*, 157–187. [CrossRef]
14. Sukharev, M.; Malinovskaya, S.A. Stimulated Raman adiabatic passage as a route to achieving optical control in plasmonics. *Phys. Rev. A* **2012**, *86*, 043406. [CrossRef]
15. Versteeg, R.B.; Zhu, J.; Padmanabhan, P.; Boguschewski, C.; German, R.; Goedecke, M.; Becker, P.; Van Loosdrecht, P. A tunable time-resolved spontaneous Raman spectroscopy setup for probing ultrafast collective excitation and quasiparticle dynamics in quantum materials. *Struct. Dyn.* **2018**, *5*, 044301. [CrossRef] [PubMed]
16. Giordmaine, J.A.; Kaiser, W. Light Scattering by Coherently Driven Lattice Vibrations. *Phys. Rev.* **1966**, *144*, 676. [CrossRef]
17. Bhupathiraju, K.V.; Seymour, A.D.; Ganikhanov, F. Femtosecond optical parametric oscillator based on periodically poled stoichiometric $LiTaO_3$ crystal. *Opt. Lett.* **2009**, *34*, 2093–2095. [CrossRef]
18. Rowley, J.D.; Yang, S.; Ganikhanov, F. Power and tuning characteristics of a broadly tunable femtosecond optical parametric oscillator base on periodically poled stoichiometric lithium tantalate. *J. Opt. Soc. Am. B* **2011**, *28*, 1026–1036. [CrossRef]

19. Sylvester, J.; Neupane, C.P.; Singhapurage, H.A.S.; Senarathna, R.M.D.M.; Sharma, G.P.; Ganikhanov, F. Femtosecond coherent Raman system with >75 dB dynamic range for probing vibration modes across 250–2400 cm^{-1}. *Opt. Express* **2022**, *30*, 23930. [CrossRef]
20. Boyd, R.W. *Nonlinear Optics*; Academic Press: Cambridge, MA, USA, 2020.
21. Menendez, J.; Cardona, M. Temperature dependence of the first-order Raman scattering by phonons in Si, Ge, and a-Sn: Anharmonic effects. *Phys. Rev. B* **1984**, *29*, 2051. [CrossRef]
22. Stanislavchuk, T.; Sirendo, A.; Litvinchuk, A.; Luo, X.; Cheong, S.W. Electronic band structure and optical phonons of $BaSnO_3$ and Ba0:97La0:03SnO3 single crystals: Theory and experiment. *J. Appl. Phys.* **2012**, *112*, 044108. [CrossRef]
23. Licheron, M.; Jouan, G.; Husson, E. Characterization of BaSnO3 powder obtained by a modified sol-gel route. *J. Eur. Ceram. Soc.* **1997**, *17*, 1453–1457. [CrossRef]
24. Perry, C.H.; Fertel, J.H.; McNelly, T.F. Temperature Dependence of the Raman Spectrum of $SrItO_3$ and $KTaO_3$. *J. Chem. Phys.* **1967**, *47*, 1619. [CrossRef]
25. Nilsen, W.G.; Skinner, J.G. Raman Spectrum of Strontium Titanate. *J. Chem. Phys.* **1968**, *48*, 2240. [CrossRef]
26. Chapron, D.; Cordero, F.; Fontana, M.D. Characterization of oxygen vacancies in $SrTiO_3$ by means of anelastic and Raman spectroscopy. *J. Appl. Phys.* **2019**, *126*, 154101. [CrossRef]
27. Kugel, G.E.; Brehatt, F.; Wyncket, B.; Fontana, M.D.; Marniers, G.; Carabatos-Nedelect, C.; Mangin, J. The vibrational spectrum of a $KTiOPO_4$ single crystal studied by Raman and infrared reflectivity spectroscopy. *Jour. Phys. C* **1988**, *21*, 5565. [CrossRef]
28. Watson, G.H. Polarized Raman spectra of ktioaso4 and isomorphic nonlinear-optical crystals. *J. Raman Spectrosc.* **1988**, *22*, 705–713. [CrossRef]
29. Shneck, R.Z.; Argaman, U.; Burshtein, Z. Anomalous LO-TO splitting observed by combined IR reflectance and Raman scattering in $KTiOPO_4$ (KTP) single crystal. *Vib. Spectrosc.* **2022**, *121*, 103385. [CrossRef]
30. Yang, S.; Ganikhanov, F. Dispersion of the resonant nonlinear optical susceptibility obtained with femtosecond time-domain Coherent Anti-Stokes Raman Scattering. *Opt. Lett.* **2013**, *38*, 4754–4757. [CrossRef]